

Colloidal Magnus effect in polymer solutions

Marco De Corato*

Aragon Institute of Engineering Research (I3A), University of Zaragoza, Zaragoza, Spain

Kun Zhang and Lailai Zhu[†]

Department of Mechanical Engineering, National University of Singapore, Singapore, Singapore

(Dated: February 26, 2025)

Rotating particles moving in fluids undergo a transverse migration via the inertia-induced Magnus effect. This phenomenon vanishes at colloidal scales because inertia is negligible and the fluid flow is time reversible. Yet, recent experiments discovered an inverse Magnus effect of colloids in polymeric and micellar solutions supposedly because their viscoelasticity breaks the time reversibility. Our study shows that classical viscoelastic features—normal-stress differences and/or shear-thinning cannot explain this phenomenon. Instead, it originates from local polymer density inhomogeneities due to their stress-gradient-induced transport, a mechanism increasingly important at smaller scales—indeed relevant to colloidal experiments. Incorporating this mechanism into our model leads to quantitative agreement with the experiments without fitting parameters. Our work provides new insights into colloidal motion in complex fluids with microstructural inhomogeneities, offers a simple mechanistic theory for predicting the resulting migration, and underscores the necessity of assimilating these findings in future designs of micro-machinery including swimmers, actuators, rheometers, and so on.

The viscoelasticity of polymeric fluids enables them to exhibit effects that are often distinct or even contrary to those triggered by weak or intermediate inertia in Newtonian fluids. Consider a macroscopic object forced to move in water; removing the forcing suddenly, it continues to cruise forward due to inertia. Conversely, a colloid in viscoelastic fluids moves backward upon force removal—a phenomenon termed recoil in microrheology [1]. Another example is the rod-climbing or “Weissenberg” effect [2], where the free surface of a complex fluid climbs up a spinning rod, whereas the near-rod surface would bend down in Newtonian fluids with inertia. Similarly, while inertia drives the wind from the poles to the equator at the scale of the rotating Earth, desktop experiments [3, 4] showcased a reversely-directed secondary flow around a rotating sphere in polymeric liquids.

Recent experiments [5] presented another compelling illustration of this contrasting trend. As depicted in Figure 1(b), a spinning and translating micron-sized colloidal particle in micellar solutions with negligible inertia was observed migrating perpendicular to both its spinning and translational axes. Intriguingly, the transversal migration was oriented opposite to that observed in inertial Newtonian fluids—a phenomenon commonly known as the Magnus effect [6, 7]. Such an inverse Magnus migration disappears when driving the colloid in a Newtonian fluid [see Figure 1(a)], as forbidden by the time-reversibility of the Stokes flow.

Fluid viscoelasticity is known to break the time-reversibility, allowing micron-sized particles to migrate across streamlines within complex fluids. Since its first observation by Karnis and Mason [8], viscoelasticity-induced particulate migration has been widely reported [9–15]. Typically, it originates from normal stress differences associated with non-uniform shear rates

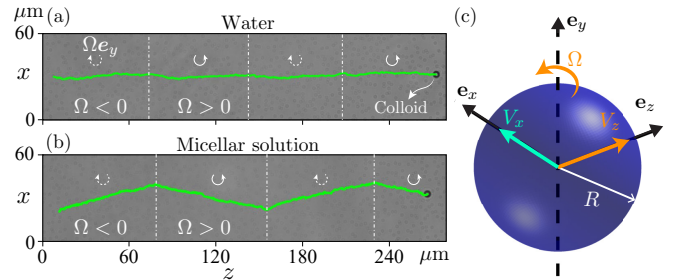


FIG. 1. Experiments demonstrate that a colloid spinning about e_y and translating along e_z in (a) water exhibits negligible lateral (e_x) motion; Contrastingly, it experiences an inverse Magnus effect in (b) a micellar solution, adapted from Cao *et al.* [5]. (c), Schematic of our model: a spherical particle with a prescribed translational velocity V_z and rotational velocity V_x , with its migration velocity V_x to be determined.

and/or geometric asymmetries, as exemplified by the lateral motion of particles towards the centerline of a Poiseuille flow and the outer wall of a rotating Couette flow [9, 10, 16]. These findings have spurred research into viscoelastic microfluidics for particle manipulation [13, 14, 17–28] and material property measurements [29]. Another example is the horizontal drift of a sedimenting colloid along the flow or gradient direction of a shear flow [30–32], driven by local variations in shear rate induced by the colloid’s translation. Beyond these scenarios with an ambient flow, normal stress imbalances owing to geometric asymmetry can enable spinning [33–35] or swinging [36] objects to propel in quiescent environments. Does the colloidal Magnus migration uncovered by Cao *et al.* [5] fit into the established categories or share any mechanistic similarities with these phenomena?

In this work, we elucidate the mechanism behind the novel Magnus effect [5] by theoretically and numerically solving the fluid flow and rheological constitutive equations. We find that the normal stress difference and/or shear thinning, typical of polymer solutions, cannot explain the Magnus migration. This finding contrasts with the above-mentioned studies that typically link similar low-Reynolds-number colloidal migration in viscoelastic media to their normal stress differences. Crucially, we identify, through asymptotic analysis and simulations, the flow-induced inhomogeneous distribution of polymers as an indispensable enabler for the new Magnus effect—a mechanism previously overlooked in colloidal dynamics. Importantly, our asymptotic prediction of the Magnus effect quantitatively aligns with experimental data [5].

We consider a spherical particle of radius R suspended in a polymer solution. The particle is centered within a Cartesian coordinate system, as illustrated in Figure 1(c). It rotates steadily around the y -axis with angular velocity $\Omega \mathbf{e}_y$ while simultaneously translating along the z -axis at a constant velocity V_z . Due to the Magnus effect, the particle might migrate transversely, *i.e.*, in the x -direction. This corresponding transversal velocity V_x remains to be determined as part of the solution.

By neglecting the particle and fluid inertia, the governing equations for the velocity \mathbf{v} and pressure p of the polymeric flow are

$$\nabla \cdot \mathbf{v} = 0, \quad \nabla \cdot (2\eta_s \mathbf{D} - p\mathbf{I} + \boldsymbol{\tau}) = \mathbf{0}, \quad (1)$$

where η_s is the solvent viscosity, $\mathbf{D} = [\nabla \mathbf{v} + (\nabla \mathbf{v})^T]/2$ the strain-rate tensor, and $\boldsymbol{\tau}$ the polymeric stress. Far from the particle, the fluid velocity $\mathbf{v} = -V_z \mathbf{e}_z - V_x \mathbf{e}_x$. At the surface \mathcal{S} of the particle, $\mathbf{v} = \Omega \mathbf{e}_y \times \mathbf{r}$, where \mathbf{r} is the position vector. To determine the migration velocity V_x , we apply the force-free condition that the total hydrodynamic force exerted on the particle vanishes in the x -direction, namely, $\int_{\mathcal{S}} (2\eta_s \mathbf{D} - p\mathbf{I} + \boldsymbol{\tau}) : \mathbf{n} \mathbf{e}_x d\mathcal{S} = 0$, where \mathbf{n} denotes the fluid-pointing unit normal.

To model the polymeric flow, we first attempt the widely-employed Oldroyd-B (OB) constitutive equation [37–39], which represents polymers as linear elastic dumbbells with a spring constant k . The polymers are homogeneously distributed in a Newtonian solvent, with a uniform number density $n = n_\infty$, where n_∞ is the constant far-field density. The polymeric stress $\boldsymbol{\tau} = k \mathbf{C} - k_B T n \mathbf{I}$ scales linearly with the deviation of the density-weighted chain conformation \mathbf{C} from its thermal equilibrium. Here, k_B indicates the Boltzmann constant, and T is the absolute temperature. The governing equation for \mathbf{C} is [40]:

$$\lambda \overset{\nabla}{\mathbf{C}} + \mathbf{C} - \frac{k_B T}{k} n \mathbf{I} = \mathbf{0}, \quad (2)$$

with λ the relaxation time of the polymers and the upper convected derivative defined as $\overset{\nabla}{\mathbf{C}} = \frac{\partial \mathbf{C}}{\partial t} + \mathbf{v} \cdot \nabla \mathbf{C} - (\nabla \mathbf{v})^T \cdot \mathbf{C}$.

$\mathbf{C} - \mathbf{C} \cdot \nabla \mathbf{v}$.

Scaling lengths, velocities, and time by R , V_z , and V_z/R , respectively, we non-dimensionalize the governing equations, yielding three dimensionless parameters: (i) the Deborah number $De = \lambda V_z/R$ characterizing the polymer relaxation time λ to the rate of deformation; (ii) the ratio of the solvent viscosity η_s to the total viscosity, $\beta = \eta_s/(\eta_s + \eta_{p,\infty})$, where $\eta_{p,\infty} = n_\infty \lambda k_B T$ is the far-field polymeric viscosity; and (iii) the ratio of the rotational tangential velocity (from colloidal rotation) to the translational velocity, $\Omega^* = \Omega R/V_z$. Dimensionless variables are marked with asterisks hereafter.

Since the experiments showed a quadratic relationship $V_x \propto -\Omega V_z$ [5], we expect a perturbation expansion of Eqs. (1) and (2), valid for $De \ll 1$, to yield a similar scaling. To zeroth-order in De , the flow and stress fields are linearly proportional to the velocity, and the Magnus effect is forbidden. To first order in De , these fields are quadratic in the velocity and we may expect a nonzero migration velocity V_x . By performing the expansion up to this order, we obtain $V_x^* = De V_{x,1}^* + \mathcal{O}(De^2)$, and then determine the first-order correction $V_{x,1}^*$ using the Lorentz reciprocal theorem [11, 41], see End Matter (EM). Surprisingly, we find $V_{x,1}^* = 0$, consistent with numerical solutions to Eqs. (1) and (2) obtained by a finite element method [FEM, see (EM)], indicating no transversal migration. We conclude that the OB model—encompassing viscoelastic memory and the first normal stress difference—cannot account for the Magnus effect observed experimentally. Employing the Giesekus model [38] that extends the OB model by incorporating a second normal stress difference and shear-thinning properties, also fails to explain the colloidal migration (see EM).

This discrepancy with the experiments prompts a reevaluation of whether the assumptions inherent in the OB model align with the experimental conditions. Specifically, we reconsider the presumed homogeneous distribution of macromolecules. The original OB model assumes that the transport of macromolecules with a diffusion coefficient of D is dominated by advection, namely, the Péclet number $Pe = V_z R/D \rightarrow \infty$. In the large Pe limit, advection homogenizes the macromolecular distribution. However, this might not be true for flows past micron-sized objects such as those used in the experiments. At small scales, the polymers can be sufficiently extended to feel the curvature of the streamlines around the colloid and the resulting gradients of stress drive the transport of polymers [42–46]. If the rate of stress-gradient-induced transport is faster or comparable to advection, then the polymers will be distributed inhomogeneously. The relative importance of advection to the stress-gradient-induced transport is quantified by the ratio $Pe/De = R^2/\lambda D$ [47]. For a given polymer solution, this ratio depends on the particle size only. For $Pe/De \gg 1$, advection dominates and the OB model is applicable, while for $Pe/De \lesssim 1$, we expect considerable

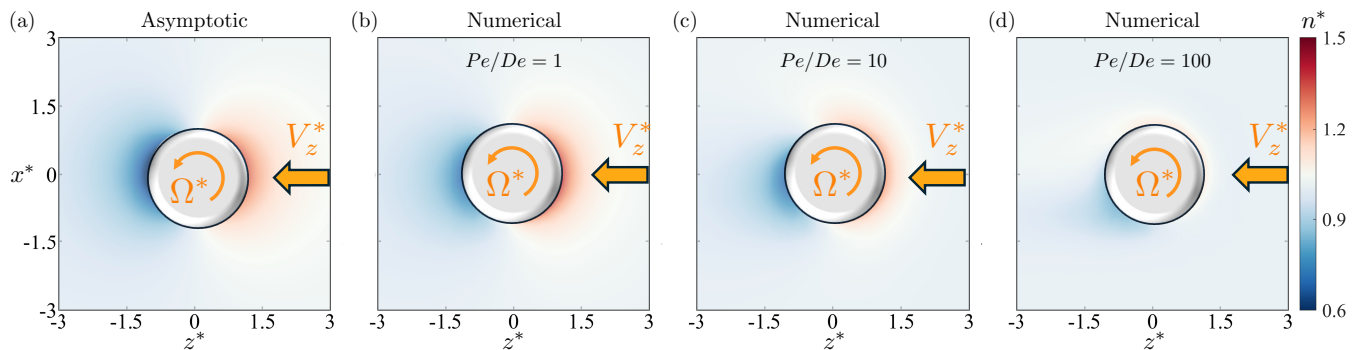


FIG. 2. Distributions of polymer number density n^* in the symmetry plane $y^* = 0$. (a), Asymptotic formula Eq. (4) at $De = 0.3$. (b-c), Numerical results at increasing Pe/De values. When $Pe/De \gg 1$, advection dominates, leading the polymer distribution to approach a homogeneous state. The remaining parameters are $\Omega^* = 0.5$, $De = 0.3$, and $\beta = 0.1$.

polymer inhomogeneities. By using a characteristic value of diffusion coefficient $D \approx 10^{-12} \text{ m}^2 \text{ s}^{-1}$ and the experimental values $R \approx 2 \mu\text{m}$ and $\lambda \approx 1 - 10 \text{ s}$ [5, 48], we estimate $Pe/De \approx 4 - 0.4$, indeed suggesting that stress-gradient-induced transport of polymers is comparable or even stronger than advection in the experiments.

Consequently, we incorporate this effect following Refs. [40, 47]. We treat the number density of polymers, n , as a variable that satisfies

$$\frac{\partial n}{\partial t} + \mathbf{v} \cdot \nabla n = D \nabla \cdot \left(\nabla n - \frac{1}{k_B T} \nabla \cdot \boldsymbol{\tau} \right), \quad (3)$$

where the rightmost term models the flux of polymer molecules driven by the gradient of the polymeric stress [40]. Accordingly, the polymer viscosity $\eta_p = n \lambda k_B T$ varies spatio-temporally. The far-field density remains as $n = n_\infty$, while polymers cannot penetrate the particle surface, where $(\nabla n - \nabla \cdot \boldsymbol{\tau} / k_B T) \cdot \mathbf{n} = 0$. We make the number density dimensionless using n_∞ , *i.e.*, $n^* = n/n_\infty$ and report the full dimensionless equations in the EM.

We perform a perturbation expansion of Eqs. (1) to (3), valid for small De and Pe numbers (see EM). To first order in De and Pe , we identify an inhomogeneous distribution of number density,

$$n^* = 1 + \frac{3De z^*}{2(r^*)^3} + \mathcal{O}(De^2, De Pe), \quad (4)$$

where r^* is the dimensionless distance from the origin. Notably, the first-order density deviation, $3De z^* / 2(r^*)^3$, from the far-field state $n_\infty^* = 1$ depends solely on De , and is independent of the rotational rate, Ω . Linearly proportional to z^* , this deviation indicates a dipolar distribution of polymers, revealing their accumulation at the front ($z^* > 0$) and depletion at the rear ($z^* < 0$) of the moving particle, see Figure 2(a). This distribution is confirmed by FEM-based numerical solutions (see EM) to Eqs. (1) to (3), as illustrated in Figure 2. The asymptotic solution, Eq. (4) agrees with simulations up

to $Pe/De \approx 10$ for $De = 0.3$ and $\Omega^* = 0.5$. Remarkably, the perturbation expansion remains valid even when flow advection exceeds stress-gradient-induced transport of polymers. At large Pe/De , the concentration dipole tilts away from the colloid's translational orientation (\mathbf{e}_z) [see Figure 2(c-d)], a signature of growing rotational convection effect—as also identified by Cao *et al.* [5].

By further extending the asymptotic analysis through the Lorentz reciprocal theorem, we derive the leading-order transversal velocity of the colloid, signifying the Magnus effect (see EM):

$$V_x^* = -\frac{(1 - \beta) De \Omega^*}{4} \quad (5)$$

with its dimensional form:

$$V_x = -\frac{\lambda \eta_{p,\infty} V_z \Omega}{4(\eta_s + \eta_{p,\infty})}. \quad (6)$$

This asymptotic prediction captures the experimentally identified trend, $V_x/V_z = -\alpha \Omega$ (where $\alpha > 0$) [5], in both sign and scaling, as further examined below. Moreover, Eq. (5) is cross-validated against FEM simulations, as evidenced in Figure 3. In the weak rotation limit, $\Omega^* \ll 1$, the numerical and theoretical data match closely for small De (*e.g.*, 0.1) and Pe/De (*e.g.*, 0.1 and 1). However, deviations emerge when $De \geq 0.3$, and systematically grow with Ω^* . Evidently, as the colloid spins faster, the numerical results fall increasingly below the linear asymptotic trend. Specifically at $De = 0.3$, they approach a saturated value when $Pe/De = 0.1$ [Figure 3(a)] or 1 [Figure 3(b)], resonating the velocity saturation reported in the experiments [5].

Additionally, Figure 3(d) reveals the Magnus velocity $-V_x^*$ versus De at a spinning rate of $\Omega^* = 0.5$. The velocity decreases with increasing Pe/De , eventually becoming negligible when $Pe/De = 100$. Indeed, in this regime of dominant advection, the OB model is recovered, resulting in no colloid migration, as we find in our initial attempt. In the opposite limit $Pe/De = 0.1$ (weak advective

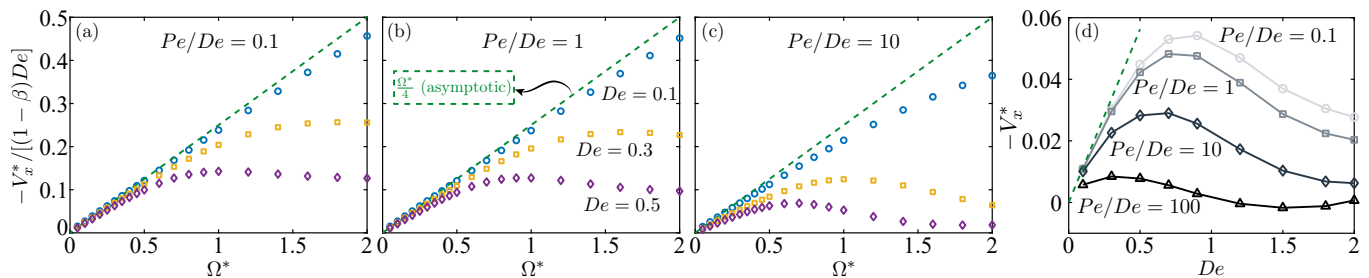


FIG. 3. Numerical Magnus velocity $-V_x^*$ compared to the asymptotic prediction Eq. (5) versus the particle's dimensionless spinning rate Ω^* , when the ratio of advection to stress-gradient-induced transport is (a) weak, $Pe/De = 0.1$; (b) intermediate, $Pe/De = 1$; and (c) strong, $Pe/De = 10$. (d), $-V_x^*$ versus De at four Pe/De values when $\Omega^* = 0.5$. Here, $\beta = 0.1$.

tion), simulations quantitatively reproduce the asymptotic linear dependence of $-V_x^*$ on De at low values of De . Beyond that regime, the velocity changes non-monotonically with De and peaks at $De \approx 1$. Notably, such a peak was reported in studies of micro-locomotion in viscoelastic fluids [49, 50].

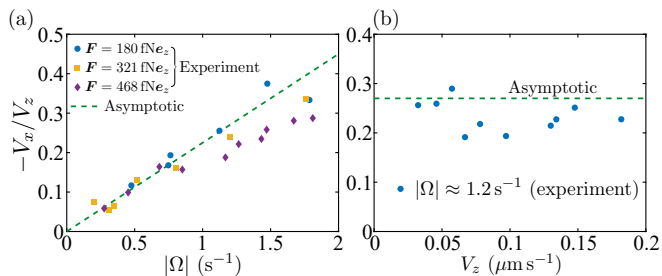


FIG. 4. Quantitative agreement (using no fitting parameters) between our asymptotic prediction, Eq. (6), and the experimental results [5] for a rotating trimer in a micellar solution, see Figure 1(b). It experienced (a) three z -oriented forces \mathbf{F} with various rotating speeds $|\Omega|$, and (b) varying translational velocities V_z at a prescribed $|\Omega| \approx 1.2 \text{ s}^{-1}$.

We now apply the numerically-validated theory to characterize the experimental observations of Cao *et al.* [5] on colloidal trimers in a micellar solution. Its rheological properties, measured and previously reported by the same group [48], make this characterization possible. Particularly, these properties include $\lambda \approx 0.9 \text{ s}$ (see EM) and $\eta_{p,\infty}/(\eta_s + \eta_{p,\infty}) \rightarrow 1$ (see EM). Substituting them into Eq. (6), a quantitative agreement emerges between the theory and experiments in Figure 4(a), where the trimers were forced to translate at three speeds and spin at various rates. A similar agreement holds for a trimer spinning at $|\Omega| \approx 1.2 \text{ s}^{-1}$ but translating at various speeds, as depicted in Figure 4(b). Remarkably, this agreement does not rely on any fitting parameters. Admittedly, the asymptotic prediction overestimates the Magnus effect of strong spinners (large Ω)—a discrepancy that grows more pronounced at higher translational velocities V_z (subject to the increased e_z -oriented force \mathbf{F}). In fact, numerical data in Figure 3(a-c) have revealed a

similar deviation, where a larger $De = \lambda V_z/R$ in simulations corresponds to a higher V_z in experiments. Indeed, as De increases, higher-order effects become increasingly important, leading to larger deviations. Note that in the experiment the authors used a trimer, while we consider a sphere here.

Based on our findings, we attribute the experimentally observed Magnus effect to two mechanisms. First, the colloidal translation and the concomitant stress-gradient-induced transport cause the polymer concentration n to be higher at the front but lower at the rear of the colloid, yielding a dipolar distribution of polymeric viscosity $\eta_p = n\lambda k_B T$ around it. Second, the colloidal rotation in such a viscosity profile results in a fore-aft stress imbalance, driving the transversal migration. Indeed, the migration velocity, Eq. (5), is identical to that of a sphere rotating in a Newtonian fluid with a dipolar distribution of viscosity [51]. This analogy indirectly suggests that the Magnus effect stems purely from the spatial viscosity variation due to an inhomogeneous polymer distribution. Normal stress differences and shear-thinning might play a secondary role, likely becoming important at much higher De numbers. These findings align with recent studies highlighting the importance of local microstructure and viscosity inhomogeneities in the dynamics of active particles [52–59].

Conclusions—We have established that the inverse Magnus migration of a colloid, experimentally observed in polymeric solutions [5], cannot be explained by normal stress differences or shear-thinning rheology. Instead, our analysis reveals that stress-gradient-induced polymer transport and the ensuing local viscosity variations underlie the observed migration. This mechanistic interpretation is validated by the striking quantitative agreement between experimental data and our theoretical model, which incorporate these mechanisms—notably, without adjustable parameters. Critically, our results underscore the necessity of reassessing standard constitutive models predicated on homogeneous polymer distributions, both for modeling colloidal dynamics in complex fluids and, more broadly, in (sub)micro-scale polymeric flows. In these cases, macromolecules can feel the curvature of the

streamlines leading to significant concentration inhomogeneities, which can play a more important role than viscoelastic stresses.

MDC was supported by the Ramon y Cajal fellowship RYC2021-030948-I and by the PID2022-139803NB-I00 research grant funded by the MICIU/AEI/10.13039/501100011033 and by the EU under the NextGenerationEU/PRTR program. LZ acknowledges the support from the Singapore Ministry of Education Academic Research Fund Tier 2 grant (MOE-T2EP50221-0012 and MOE-T2EP50122-0015). Some computation of the work was performed on resources of the National Supercomputing Centre, Singapore (<https://www.nsc.sg>). We thank Xin Cao for initial discussions and Hua Zhang for performing some preliminary simulations. MDC and LZ thank Eric Keaveny, Blaise Delmotte, and the European Mechanics Society for the invitation to the 645 EUROMECH Colloquium on Non-linear Dynamics at Zero Reynolds Numbers, which fostered this collaboration.

* mdecorato@unizar.es

† lailai_zhu@nus.edu.sg

- [1] C. D. Chapman and R. M. Robertson-Anderson, Nonlinear microrheology reveals entanglement-driven molecular-level viscoelasticity of concentrated DNA, *Phys. Rev. Lett.* **113**, 098303 (2014).
- [2] K. Weissenberg, A continuum theory of rheological phenomena, *Nature* **159**, 310 (1947).
- [3] H. Giesekus, Some secondary flow phenomena in general viscoelastic fluids, in *Proc. 4th Intern. Congr. Rheology, Part 1* (1965).
- [4] C. T. Hill, Nearly viscometric flow of viscoelastic fluids in the disk and cylinder system. II: Experimental, *Trans. Soc. Rheol.* **16**, 213 (1972).
- [5] X. Cao, D. Das, N. Windbacher, F. Ginot, M. Krüger, and C. Bechinger, Memory-induced Magnus effect, *Nat. Phys.* **19**, 1904 (2023).
- [6] I. Newton, A new theory about light and colors, *Am. J. Phys.* **61**, 108 (1993).
- [7] G. Magnus, Ueber die Abweichung der Geschosse, und: Ueber eine auffallende Erscheinung bei rotirenden körpern, *Ann. Phys. (Berl.)* **164**, 1 (1853).
- [8] A. Karnis and S. G. Mason, Particle motions in sheared suspensions. XIX. Viscoelastic media, *Trans. Soc. Rheol.* **10**, 571 (1966).
- [9] B. P. Ho and G. Leal, Migration of rigid spheres in a two-dimensional unidirectional shear flow of a second-order fluid, *J. Fluid Mech.* **76**, 783 (1976).
- [10] P. C.-H. Chan and L. G. Leal, A note on the motion of a spherical particle in a general quadratic flow of a second-order fluid, *J. Fluid Mech.* **82**, 549 (1977).
- [11] L. G. Leal, The motion of small particles in non-Newtonian fluids, *J. Non-Newton. Fluid Mech.* **5**, 33 (1979).
- [12] P. Brunn, The motion of rigid particles in viscoelastic fluids, *J. Non-Newtonian Fluid Mech.* **7**, 271 (1980).
- [13] A. M. Leshansky, A. Bransky, N. Korin, and U. Dinnar, Tunable nonlinear viscoelastic “focusing” in a microfluidic device, *Phys. Rev. Lett.* **98**, 234501 (2007).
- [14] G. D’Avino, F. Greco, and P. L. Maffettone, Particle migration due to viscoelasticity of the suspending liquid and its relevance in microfluidic devices, *Annu. Rev. Fluid Mech.* **49**, 341 (2017).
- [15] D. Yuan, Q. Zhao, S. Yan, S.-Y. Tang, G. Alici, J. Zhang, and W. Li, Recent progress of particle migration in viscoelastic fluids, *Lab Chip* **18**, 551 (2018).
- [16] P. Brunn, The slow motion of a sphere in a second-order fluid, *Rheol. Acta* **15**, 163 (1976).
- [17] J. Michele, R. Pätzold, and R. Donis, Alignment and aggregation effects in suspensions of spheres in non-Newtonian media, *Rheol. Acta* **16**, 317 (1977).
- [18] G. D’Avino, F. Snijkers, R. Pasquino, M. A. Hulsen, F. Greco, P. L. Maffettone, and J. Vermant, Migration of a sphere suspended in viscoelastic liquids in Couette flow: experiments and simulations, *Rheol. Acta* **51**, 215 (2012).
- [19] J. Y. Kim, S. W. Ahn, S. S. Lee, and J. M. Kim, Lateral migration and focusing of colloidal particles and DNA molecules under viscoelastic flow, *Lab Chip* **12**, 2807 (2012).
- [20] S. Van Loon, J. Fransaer, C. Clasen, and J. Vermant, String formation in sheared suspensions in rheologically complex media: The essential role of shear thinning, *J. Rheol.* **58**, 237 (2014).
- [21] H. Lim, J. Nam, and S. Shin, Lateral migration of particles suspended in viscoelastic fluids in a microchannel flow, *Microfluid. Nanofluid.* **17**, 683 (2014).
- [22] E. J. Lim, T. J. Ober, J. F. Edd, S. P. Desai, D. Neal, K. W. Bong, P. S. Doyle, G. H. McKinley, and M. Toner, Inertio-elastic focusing of bioparticles in microchannels at high throughput, *Nat. Commun.* **5**, 4120 (2014).
- [23] K. W. Seo, H. J. Byeon, H. K. Huh, and S. J. Lee, Particle migration and single-line particle focusing in microscale pipe flow of viscoelastic fluids, *RSC Adv.* **4**, 3512 (2014).
- [24] G. Li, G. H. McKinley, and A. M. Ardekani, Dynamics of particle migration in channel flow of viscoelastic fluids, *J. Fluid Mech.* **785**, 486 (2015).
- [25] X. Lu, C. Liu, G. Hu, and X. Xuan, Particle manipulations in non-Newtonian microfluidics: A review, *J. Colloid Interface Sci.* **500**, 182 (2017).
- [26] N. O. Jaensson, C. Mitrias, M. A. Hulsen, and P. D. Anderson, Shear-induced migration of rigid particles near an interface between a Newtonian and a viscoelastic fluid, *Langmuir* **34**, 1795 (2018).
- [27] Z. Yu, P. Wang, J. Lin, and H. H. Hu, Equilibrium positions of the elasto-inertial particle migration in rectangular channel flow of Oldroyd-B viscoelastic fluids, *J. Fluid Mech.* **868**, 316 (2019).
- [28] J. Zhou and I. Papautsky, Viscoelastic microfluidics: Progress and challenges, *Microsyst. Nanoeng.* **6**, 113 (2020).
- [29] F. Del Giudice, S. J. Haward, and A. Q. Shen, Relaxation time of dilute polymer solutions: A microfluidic approach, *J. Rheol.* **61**, 327 (2017).
- [30] R. Vishnampet and D. Saintillan, Concentration instability of sedimenting spheres in a second-order fluid, *Phys. Fluids* **24** (2012).
- [31] J. Einarsson and B. Mehlig, Spherical particle sedimenting in weakly viscoelastic shear flow, *Phys. Rev. Fluids* **2**, 063301 (2017).
- [32] A. Zhang, W. L. Murch, J. Einarsson, and E. S. G.

- Shaqfeh, Lift and drag force on a spherical particle in a viscoelastic shear flow, *J. Non-Newton. Fluid Mech.* **280**, 104279 (2020).
- [33] O. S. Pak, L. Zhu, L. Brandt, and E. Lauga, Micropropulsion and microrheology in complex fluids via symmetry breaking, *Phys. Fluids* **24** (2012).
- [34] Y. Su, A. Castillo, O. S. Pak, L. Zhu, and R. Zenit, Viscoelastic levitation, *J. Fluid Mech.* **943**, A23 (2022).
- [35] L. A. Kroo, J. P. Binagia, N. Eckman, M. Prakash, and E. S. G. Shaqfeh, A freely suspended robotic swimmer propelled by viscoelastic normal stresses, *J. Fluid Mech.* **944**, A20 (2022).
- [36] D. A. Gagnon, N. C. Keim, X. Shen, and P. E. Arratia, Fluid-induced propulsion of rigid particles in wormlike micellar solutions, *Phys. Fluids* **26** (2014).
- [37] R. B. Bird, R. C. Armstrong, and O. Hassager, *Dynamics of Polymeric Liquids. Vol. 1: Fluid Mechanics* (John Wiley and Sons Inc., New York, NY, 1987).
- [38] R. G. Larson, *Constitutive Equations for Polymer Melts and Solutions: Butterworths Series in Chemical Engineering* (Butterworth-Heinemann, 2013).
- [39] A. Morozov and S. E. Spagnolie, Introduction to complex fluids, in *Complex Fluids in Biological Systems: Experiment, Theory, and Computation*, edited by S. E. Spagnolie (Springer New York, New York, NY, 2015) pp. 3–52.
- [40] M. V. Apostolakis, V. G. Mavrantzas, and A. N. Beris, Stress gradient-induced migration effects in the Taylor–Couette flow of a dilute polymer solution, *J. Non-Newtonian Fluid Mech.* **102**, 409 (2002).
- [41] H. Masoud and H. A. Stone, The reciprocal theorem in fluid dynamics and transport phenomena, *J. Fluid Mech.* **879**, P1 (2019).
- [42] J. H. Aubert and M. Tirrell, Macromolecules in nonhomogeneous velocity gradient fields, *J. Chem. Phys.* **72**, 2694 (1980).
- [43] E. Helfand and G. H. Fredrickson, Large fluctuations in polymer solutions under shear, *Phys. Rev. Lett.* **62**, 2468 (1989).
- [44] M. Doi, Effects of viscoelasticity on polymer diffusion, in *Dynamics and Patterns in Complex Fluids: New Aspects of the Physics-Chemistry Interface* (Springer, 1990) pp. 100–112.
- [45] S. T. Milner, Hydrodynamics of semidilute polymer solutions, *Phys. Rev. Lett.* **66**, 1477 (1991).
- [46] V. G. Mavrantzas and A. N. Beris, Modeling of the rheology and flow-induced concentration changes in polymer solutions, *Phys. Rev. Lett.* **69**, 273 (1992).
- [47] S. Tsouka, Y. Dimakopoulos, V. Mavrantzas, and J. Tsamopoulos, Stress-gradient induced migration of polymers in corrugated channels, *J. Rheol.* **58**, 911 (2014).
- [48] J. R. Gomez-Solano and C. Bechinger, Transient dynamics of a colloidal particle driven through a viscoelastic fluid, *New J. Phys.* **17**, 103032 (2015).
- [49] J. Teran, L. Fauci, and M. Shelley, Viscoelastic fluid response can increase the speed and efficiency of a free swimmer, *Phys. Rev. Lett.* **104**, 038101 (2010).
- [50] B. Liu, T. R. Powers, and K. S. Breuer, Force-free swimming of a model helical flagellum in viscoelastic fluids, *Proc. Natl. Acad. Sci. USA* **108**, 19516 (2011).
- [51] N. Oppenheimer, S. Navardi, and H. A. Stone, Motion of a hot particle in viscous fluids, *Phys. Rev. Fluids* **1**, 014001 (2016).
- [52] B. Liebchen, P. Monderkamp, B. Ten Hagen, and H. Löwen, Viscotaxis: Microswimmer navigation in viscosity gradients, *Phys. Rev. Lett.* **120**, 208002 (2018).
- [53] C. Datt and G. J. Elfring, Active particles in viscosity gradients, *Phys. Rev. Lett.* **123**, 158006 (2019).
- [54] R. Dandekar and A. M. Ardekani, Swimming sheet in a viscosity-stratified fluid, *J. Fluid Mech.* **895**, R2 (2020).
- [55] V. A. Shaik and G. J. Elfring, Hydrodynamics of active particles in viscosity gradients, *Phys. Rev. Fluids* **6**, 103103 (2021).
- [56] C. Esparza López, J. Gonzalez-Gutierrez, F. Solorio-Ordaz, E. Lauga, and R. Zenit, Dynamics of a helical swimmer crossing viscosity gradients, *Phys. Rev. Fluids* **6**, 083102 (2021).
- [57] M. R. Stehnach, N. Waisbord, D. M. Walkama, and J. S. Guasto, Viscophobic turning dictates microalgae transport in viscosity gradients, *Nat. Phys.* **17**, 926 (2021).
- [58] K. S. Olsen, L. Angheluta, and E. G. Flekkøy, Active Brownian particles moving through disordered landscapes, *Soft Matter* **17**, 2151 (2021).
- [59] M. De Corato and P. Martínez-Lera, Enhanced rotational diffusion and spontaneous rotation of an active Janus disk in a complex fluid, *Soft Matter* **21**, 186 (2025).

END MATTER

Here, we report the steady-state dimensionless equations and elaborate the asymptotic analysis.

Oldroyd-B (OB) and Giesekus models

Using the characteristic scales defined in the main text, we obtain the dimensionless governing equations. The momentum balance and continuity equations are

$$\nabla^* \cdot (2\beta \mathbf{D}^* - p^* \mathbf{I} + \boldsymbol{\tau}^*) = \mathbf{0} ; \quad \nabla^* \cdot \mathbf{v}^* = 0 . \quad (7)$$

The OB model for the polymeric stress is

$$De \overset{\nabla}{\boldsymbol{\tau}^*} + \boldsymbol{\tau}^* = 2(1 - \beta) \mathbf{D}^* , \quad (8)$$

and the Giesekus counterpart is

$$De \overset{\nabla}{\boldsymbol{\tau}^*} + \boldsymbol{\tau}^* + \frac{\alpha De}{1 - \beta} \boldsymbol{\tau}^* \cdot \boldsymbol{\tau}^* = 2(1 - \beta) \mathbf{D}^* , \quad (9)$$

where α must be between 0 and 1 [38]. The force-free condition is given by

$$\int_S (2\beta \mathbf{D}^* - p^* \mathbf{I} + \boldsymbol{\tau}^*) : \mathbf{n} \mathbf{e}_x dS = 0 . \quad (10)$$

The velocity far from the particle is

$$\mathbf{v}^* = -\mathbf{e}_z - V_x^* \mathbf{e}_x , \quad (11)$$

and that at the particle surface reads

$$\mathbf{v}^* = \Omega^* \mathbf{e}_y \times \mathbf{r}^* . \quad (12)$$

Perturbation expansion—We seek a solution in the form of a perturbation expansion for small De values, expanding the relevant variables as $\mathbf{v}^* = \mathbf{v}_0^* + De \mathbf{v}_1^* + \mathcal{O}(De^2)$, $p^* = p_0^* + De p_1^* + \mathcal{O}(De^2)$, $\boldsymbol{\tau}^* = \boldsymbol{\tau}_0^* + De \boldsymbol{\tau}_1^* + \mathcal{O}(De^2)$, and $V_x^* = De V_{x,1}^* + \mathcal{O}(De^2)$.

Zeroth-order problem—The zero-order equations are obtained by substituting the perturbation expansion into the main equations and retaining only the terms that do not depend on De . The polymeric stress is $\boldsymbol{\tau}_0^* = 2(1 - \beta) \mathbf{D}_0^*$. The zeroth-order momentum and continuity equations are

$$\nabla^* \cdot (2\mathbf{D}_0^* - p_0^* \mathbf{I}) = \mathbf{0} ; \quad \nabla^* \cdot \mathbf{v}_0^* = 0 , \quad (13)$$

corresponding to the Newtonian Stokes flow. Its flow field can be obtained by superimposing the flow past a sphere and that around a spinning sphere, resulting in

$$\mathbf{v}_0^* = \mathbf{e}_z \cdot \left[\left(\frac{3}{4r^*} + \frac{1}{4r^{*3}} \right) \mathbf{I} + \frac{3}{4} \left(\frac{1}{r^{*3}} - \frac{1}{r^{*5}} \right) \mathbf{r}^* \mathbf{r}^* \right] + \Omega^* \mathbf{e}_y \times \mathbf{r}^* / r^{*3} - \mathbf{e}_z . \quad (14)$$

First-order problem—The first-order equations are obtained by substituting the perturbation expansion into the equations and retaining only the terms proportional to De . The first order solution of the polymeric stress is

$$\boldsymbol{\tau}_1 = 2(1 - \beta) \mathbf{D}_1^* - \overset{\nabla}{\boldsymbol{\tau}_0^*} . \quad (15)$$

for the OB fluid and

$$\boldsymbol{\tau}_1 = 2(1 - \beta) \mathbf{D}_1^* - \overset{\nabla}{\boldsymbol{\tau}_0^*} - \frac{\alpha De}{1 - \beta} \boldsymbol{\tau}_0^* \cdot \boldsymbol{\tau}_0^* , \quad (16)$$

for the Giesekus model. The momentum and the continuity equations are

$$\nabla \cdot (2\beta \mathbf{D}_1^* - p_1^* \mathbf{I} + \boldsymbol{\tau}_1^*) = \mathbf{0} ; \quad \nabla \cdot \mathbf{v}_1^* = 0 . \quad (17)$$

The far-field velocity $\mathbf{v}_1^* = -V_{x,1}^* \mathbf{e}_x$ and $\mathbf{v}_1^* = \mathbf{0}$ at the particle surface. The first-order force-free condition is $\int_S (2\beta \mathbf{D}_1^* - p_1^* \mathbf{I} + \boldsymbol{\tau}_1^*) : \mathbf{n} \mathbf{e}_x dS = 0$.

Generalized reciprocal theorem—Using the Lorentz reciprocal theorem [11, 41], we compute the first-order velocity $V_{x,1}^*$ by the volume integral over the fluid domain, \mathcal{V} . For the OB model,

$$V_{x,1}^* = \frac{1}{6\pi} \int_{\mathcal{V}} \nabla \hat{\mathbf{v}}^* : \overset{\nabla}{\boldsymbol{\tau}_0^*} dV , \quad (18)$$

where $\hat{\mathbf{v}}^*$ is an auxiliary velocity field corresponding to Newtonian Stokes flow with an ambient velocity $1\mathbf{e}_x$ past a stationary sphere. Likewise, for the Giesekus model,

$$V_{x,1}^* = \frac{1}{6\pi} \int_{\mathcal{V}} \nabla \hat{\mathbf{v}}^* : \left(\overset{\nabla}{\boldsymbol{\tau}_0^*} - \frac{\alpha De}{1 - \beta} \boldsymbol{\tau}_0^* \cdot \boldsymbol{\tau}_0^* \right) dV . \quad (19)$$

Stress-gradient induced polymer transport

The OB and Giesekus models assume a uniform far-field number density $n = n_\infty$. Here, we extend the OB model by incorporating a nonuniform density n . Taking n_∞ as the characteristic scale, the dimensionless number density $n^* = n/n_\infty$. While the momentum and continuity equations remain unchanged, the polymeric stress follows an adapted constitutive law [40, 47]

$$De \overset{\nabla}{\boldsymbol{\tau}^*} + \boldsymbol{\tau}^* + (1 - \beta) \left(\frac{Dn^*}{Dt^*} \right) \mathbf{I} = 2(1 - \beta) n^* \mathbf{D}^* , \quad (20)$$

where $D()/Dt^*$ denotes the material derivative. Specifically, the spatio-temporal evolution of n^* is governed by

$$Pe \frac{Dn^*}{Dt} = \nabla \cdot \left(\nabla n^* - \frac{De}{1 - \beta} \nabla \cdot \boldsymbol{\tau}^* \right) . \quad (21)$$

The force-free condition and boundary conditions for the velocity are the same as Eqs. (10) to (12). The boundary condition for n^* at the particle surface reads

$$\mathbf{n} \cdot \left(-\nabla n^* + \frac{De}{1 - \beta} \nabla \cdot \boldsymbol{\tau}^* \right) = 0 , \quad (22)$$

and that far from the particle is $n^* = 1$.

Perturbation expansion—We seek a solution in the form of a perturbation expansion for small De and Pe . We find that all asymptotic terms proportional to powers of Pe only are zero. The variables are expanded as: $\mathbf{v}^* = \mathbf{v}_0^* + De \mathbf{v}_1^* + \mathcal{O}(De^2, DePe)$, $p^* = p_0^* + De p_1^* + \mathcal{O}(De^2, DePe)$, $\boldsymbol{\tau}^* = \boldsymbol{\tau}_0^* + De \boldsymbol{\tau}_1^* + \mathcal{O}(De^2, DePe)$, $n^* = 1 + De n_1^* + \mathcal{O}(De^2, DePe)$, and $V_x^* = De V_{x,1}^* + \mathcal{O}(De^2, DePe)$.

Zeroth-order problem—The zeroth-order equations and their solutions, \mathbf{v}_0^* and p_0 , are the same as those for the OB and Giesekus models because the zeroth-order polymer density is uniformly equal to its far-field value.

First-order problem—The first order polymeric stress takes the form,

$$\boldsymbol{\tau}_1^* = 2(1 - \beta) (n_1^* \mathbf{D}_0^* + \mathbf{D}_1^*) - \boldsymbol{\tau}_0^* - (1 - \beta) \left(\frac{Dn_1^*}{Dt} \right) \mathbf{I}. \quad (23)$$

We note that the last term is an isotropic tensor not contributing to the velocity field. It can be absorbed by defining a modified $P_1^* = p_1^* + (1 - \beta) Dn_1^*/Dt$, yielding

$$\boldsymbol{\tau}_1^* = 2(1 - \beta) (n_1^* \mathbf{D}_0^* + \mathbf{D}_1^*) - \boldsymbol{\tau}_0^*. \quad (24)$$

The momentum and continuity equations are $\nabla \cdot (2\beta \mathbf{D}_1^* - P_1^* \mathbf{I} + \boldsymbol{\tau}_1^*) = \mathbf{0}$; $\nabla \cdot \mathbf{v}_1^* = 0$. The velocity far from the particle is $\mathbf{v}_1^* = -V_{x,1}^* \mathbf{e}_x$ and at the particle surface $\mathbf{v}_1^* = \mathbf{0}$. The force-free condition is $\int_{S^*} (2\beta \mathbf{D}_1^* - P_1^* \mathbf{I} + \boldsymbol{\tau}_1^*) : \mathbf{n} \mathbf{x} \mathbf{e}_x dS^* = 0$. To proceed, we first solve for the number density n_1^* . Its steady-state solution follows:

$$\nabla \cdot \left(\nabla n_1^* - \frac{1}{1 - \beta} \nabla \cdot \boldsymbol{\tau}_0^* \right) = 0, \quad (25)$$

which can reduced to the Laplace equation $\nabla^2 n_1^* = 0$ realizing $\nabla \nabla : \boldsymbol{\tau}_0^* = 0$. The zero-flux boundary condition at the particle surface becomes

$$\mathbf{n} \cdot \left(-\nabla n_1^* + \frac{1}{1 - \beta} \nabla \cdot \boldsymbol{\tau}_0^* \right) = 0, \quad (26)$$

and $n_1^* = 0$ in the far field. We obtain $n_1^* = 3z^*/2r^{*3}$ that is independent of Ω^* , implying that the particle rotation does not cause the polymer inhomogeneity at the first order.

Generalized reciprocal theorem—Employing again the reciprocal theorem, we derive the first-order velocity as

$$V_{x,1}^* = \frac{1}{6\pi} \int_{\mathcal{V}} \nabla \hat{\mathbf{v}}^* : \left[2(1 - \beta) n_1^* \mathbf{D}_0^* + \boldsymbol{\tau}_0^* \right] d\mathcal{V}. \quad (27)$$

Noting that the integral involving $\boldsymbol{\tau}_0^*$ is identical to that for the OB model [see Eq. (18)] and is thus zero, the

first-order velocity is given by

$$V_{x,1}^* = \frac{1}{6\pi} \int_{\mathcal{V}} \nabla \hat{\mathbf{v}}^* : [2(1 - \beta) n_1^* \mathbf{D}_0^*] d\mathcal{V}, \quad (28)$$

which crucially depends on the first-order inhomogeneous polymer distribution n_1^* derived above.

Numerical methods

We solve the dimensionless equations using the FEM package, COMSOL Multiphysics (I-Math, Singapore), specifically employing its Partial Differential Equation Interface. Exploiting the mirror-symmetry about the x^*z^* -plane, we consider a fluid domain in the form of a semi-spherical shell with an inner radius of 1 and an outer radius of 200. The inner and outer boundaries represent the particle surface and far field, respectively. The domain is discretized by $\approx 198,000$ tetrahedral elements, with polynomial order two for velocity \mathbf{u}^* , and order one for the other variables (pressure p^* , polymeric stress $\boldsymbol{\tau}^*$, and number density n^*), respectively. The mesh is refined near the particle surface, yielding a minimum element size of 0.1. We perform a mesh-independence study, as summarized in Table I.

To stabilize the simulations, streamline diffusion is applied to the $\boldsymbol{\tau}^*$ and n^* equations. Imposing the force-free condition to compute the migration velocity of particles is achieved through a ‘Global Equations’ node. We solve the equations in a fully coupled manner, utilizing the direct solver MUMPS.

Minimum element size	Total number of elements	Migration velocity $-V_x^*$
0.2	$\approx 136,000$	0.0252
0.135	$\approx 165,000$	0.0287
0.1	$\approx 198,000$	0.0296
0.07	$\approx 262,000$	0.0298
0.05	$\approx 359,000$	0.0297

TABLE I. Mesh dependence evaluated at $\beta = 0.1$, $De = Pe = 0.3$, and $\Omega^* = 0.5$. The mesh used in our study is highlighted in gray.

Rheological properties of the micellar solution

For the theory-experiment comparison shown in Figure 4, the rheological fluid tested by Cao *et al.* [5] was a wormlike micellar solution composed of about 5 mM equimolar cetylpyridinium chloride monohydrate (CPyCl) and sodium salicylate (NaSal) dissolved in water. Its rheological properties were measured by the same group [48]. As reported, its zero-shear viscosity is 0.045 ± 0.005 Pa·s, substantially larger than the viscosity of water, thereby leading to $\beta \rightarrow 0$. The inset of Figure 6(c) in Ref. [48] indicates that the solution’s largest relaxation time is approximately 0.9s, which we choose as the relaxation time λ in our constitutive model.